Geometry-Aware Bayesian Detection of Spatially Variable Genes in Three Dimensions

Abstract

Three-dimensional spatial transcriptomics (ST) enables the direct characterization of transcriptional organization within intact tissue architecture, offering new insight into how molecular programs are structured across volumetric tissues. One key analytical task is to detect spatially variable genes (SVGs) whose expression carries location-dependent information relevant to tissue organization. However, many existing approaches describe spatial structure through prespecified kernels, covariance models, or basis systems, which can be restrictive for irregular patterns governed by complex tissue geometry. In this paper, we propose GeoSVG-3D, a fully Bayesian framework for SVG detection in three-dimensional ST data. GeoSVG-3D builds a neighborhood graph from the observed tissue geometry encoded by three-dimensional spatial coordinates and derives geometry-aware basis functions that summarize local connectivity and overall tissue organization. Within this representation, gene expression is modeled as a sparse expansion over these basis functions using neuronized priors, allowing spatial dependence to be learned from data-supported coefficients rather than prespecified pattern classes. Bayesian false discovery rate control is further applied to gene-level posterior evidence to determine the final SVG set. Both Simulation studies and real data analyses demonstrate that GeoSVG-3D successfully identifies SVGs with complex expression patterns across different settings and provides probabilistic quantification of spatial expression heterogeneity in three-dimensional tissues.

Keywords: Bayesian variable selection, geometry-aware modeling, spatial transcriptomics, spatially variable genes, three-dimensional tissue architecture

Mathematics Subject Classification (2020): 62C10

1 Introduction

Spatial transcriptomics (ST) has provided a powerful framework for characterizing gene expression within its intact tissue context. By jointly measuring molecular profiles and spatial coordinates, ST technologies enable the investigation of how transcriptional mechanisms are organized across anatomical regions, cellular neighborhoods, and tissue microenvironments (Ståhl et al., 2016; Rao et al., 2021). Recent advances in sequencing-based profiling, multiplexed in situ imaging, and computational reconstruction have further extended ST studies from two-dimensional tissue sections toward three-dimensional tissue architectures (Wang et al., 2018; Fang et al., 2024; Sui et al., 2025). Compared with analyses based on individual two-dimensional sections, three-dimensional ST data can provide a more complete representation of biological

structures and regulatory processes (Wang et al., 2023a; Schott et al., 2024), thereby creating new opportunities for studying tissue organization and spatial heterogeneity.

A fundamental task in ST analysis, and particularly in three-dimensional ST, is the detection of spatially variable genes (SVGs), namely genes whose expression exhibits systematic spatial patterns across different tissue locations (Yan et al., 2025; Li et al., 2025b). SVG detection is essential for understanding tissue organization, spatially regulated biological functions, and region-specific molecular programs (Yan et al., 2025), and has been widely applied in studies of tumors, brain tissues, developmental systems, and other spatially organized biological contexts (Zhou et al., 2023). To characterize gene-level expression variation, existing methods have typically introduced a variety of spatial dependence models, underscoring the importance of effective spatial signal representation in SVG detection. From a statistical perspective, the key challenge is to distinguish spatially informative variation from non-spatial fluctuations and technical noise in complex ST data, which highlights the need for an accurate and flexible characterization of spatial expression structures.

Despite substantial progress, many existing SVG detection methods still rely on predefined representations of spatial variation patterns. One major category of methods characterizes spatial dependence through prespecified kernels or covariance structures (Seeger, 2004; Stein, 1999). For two-dimensional ST data, SpatialDE models spatial signals using Gaussian-process covariance functions, including squared-exponential, linear, and periodic kernels (Svensson et al., 2018). SPARK directly models ST count data through generalized linear spatial models and uses multiple Gaussian and cosine kernels to capture focal and periodic expression patterns (Sun et al., 2020). More scalable extensions, such as SPARK-X, formulate SVG detection as a nonparametric covariance test between gene expression and spatial coordinates, while still employing prespecified covariance matrices and coordinate transformations to target linear, focal, and periodic spatial structures (Zhu et al., 2021). Another category of approaches specifies spatial effects through fixed basis functions, representing gene expression as a linear combination of prespecified spatial components (Cable et al., 2022; Yu and Luo, 2022; Yu and Li, 2024; Wang et al., 2025). More recently, scBSP has been proposed as a dimension-agnostic nonparametric framework, making it one of the pioneering methods for SVG detection in three-dimensional ST data (Li et al., 2025a). Rather than specifying a parametric spatial covariance structure, scBSP compares the variance of local mean expression across spatial scales and computes a gene-level p-value based on a fitted distribution (Wang et al., 2023b). Although these strategies can be effective when the chosen covariance functions, basis systems, or local-scale summaries are well matched to the underlying expression structure, spatial expression patterns in currently available three-dimensional tissue data are highly diverse and often exhibit intricate and irregular structures owing to the anatomical geometry. Therefore, developing a flexible representation that can adapt to unknown and heterogeneous spatial expression patterns remains a central challenge for SVG detection in three-dimensional ST data.

Motivated by this need, we introduce a *geometry-aware modeling* strategy for detecting SVGs in three-dimensional ST data. In this work, geometry-aware modeling refers to constructing data-driven representations of expression variation by leveraging the observed tissue geometry. Instead of manually specifying basis functions, we build a spatial graph from the

three-dimensional coordinates of cells and derive graph-based basis functions that reflect the underlying tissue architecture (Belkin and Niyogi, 2003, 2006). These basis functions encode both local neighborhood information and global structural organization (Shuman et al., 2013; Hammond et al., 2011), allowing the model to capture a broad range of spatial expression patterns. Accordingly, the proposed framework does not require prior specification of the spatial configuration of gene expression—the geometry of the tissue itself provides an adaptive foundation for modeling the expression variation.

Building upon this spatial representation, SVG detection can be naturally formulated as a basis-level variable selection problem, focusing on how to separate truly spatial components from noisy or non-spatial ones. For each gene, meaningful spatial dependence corresponds to nonzero coefficients associated with one or more geometry-derived basis functions, whereas a gene with no retained spatial component can be regarded as non-spatially variable. The inferential goal is therefore to identify which components of the adaptive basis contribute to each gene's expression structure and to use this information to determine its SVG status. In the variable selection literature, such coefficient-level selection is commonly handled through penalized estimation procedures, including Lasso-type methods (Tibshirani, 1996), elastic-net regularization (Zou and Hastie, 2005), group penalties (Yuan and Lin, 2006), and non-convex penalties such as SCAD or MCP (Fan and Li, 2001; Zhang, 2010). These methods provide computationally efficient tools for sparse coefficient estimation and have been widely used in high-dimensional regression settings. However, their selected active sets are often driven by tuning-parameter choices and are typically summarized through point estimates of the sparse coefficients. In comparison, a Bayesian framework provides a more suitable formulation for basis-level selection, as it can jointly impose sparsity and quantify posterior uncertainty in spatial-basis coefficients and gene-level spatial variability within a unified probabilistic model (O'Hara and Sillanpää, 2009). In this context, neuronized priors provide an efficient and flexible mechanism for Bayesian variable selection by shrinking negligible coefficients toward zero while retaining active spatial components (Shin and Liu, 2022). Such a formulation enables SVG identification through selected basis components and naturally provides a coherent probabilistic interpretation of spatial expression structure.

In this paper, we propose GeoSVG-3D, a Geometry-aware Bayesian method for detecting Spatially Variable Genes in Three-Dimensional ST data. To the best of our knowledge, GeoSVG-3D is the first framework that jointly (i) provides a geometry-aware Bayesian formulation specifically designed for three-dimensional ST data, (ii) uses graph-derived basis functions to flexibly model unknown spatial expression patterns without imposing restrictive assumptions on their functional form, and (iii) incorporates Bayesian neuronized priors to achieve sparse selection over spatial-basis coefficients with uncertainty quantification. Within this framework, GeoSVG-3D aggregates coefficient-level posterior information into gene-level SVG evidence and applies Bayesian false discovery rate control to determine the final selected gene set (Müller et al., 2007). Through simulation studies and real data analyses, we demonstrate that GeoSVG-3D can effectively detect SVGs and flexibly capture complex spatial signals in three-dimensional tissue structures.

2 Method

2.1 Graph Laplacian construction

Suppose that we observe a three-dimensional ST tissue block consisting of n cells and obtain a gene expression matrix for G genes. For each cell i ($i = 1, \ldots, n$), let $\mathbf{s}_i = (s_{i1}, s_{i2}, s_{i3})$ denote its three-dimensional spatial coordinate. The gene expression matrix is denoted by $\mathbf{Y} = (\mathbf{y}_1, \ldots, \mathbf{y}_G) \in \mathbb{R}^{n \times G}$, where $\mathbf{y}_g = (y_{1g}, \ldots, y_{ng})^\top$ represents the continuous expression profile of gene g, obtained from the original count data after standard preprocessing. Among these genes, SVGs are expected to show structured expression variability associated with cell locations. Such patterns may appear as periodic variation, localized activation, or other geometry-related forms, and can help reveal the complex tissue-level organization (Yu and Luo, 2022; Walker et al., 2022).

Statistically, to encode the three-dimensional tissue geometry, spatial graphs provide a natural way to represent neighborhood relationships among cells in the tissue space (Von Luxburg, 2007; Hu et al., 2021). In our framework, we first construct a weighted spatial graph from the coordinates of all cells. In this graph, each node represents a cell, and each edge weight measures the spatial proximity between two cells. Let $\mathbf{W} \in \mathbb{R}^{n \times n}$ denote the adjacency matrix, where w_{ij} is the edge weight between cells i and j. In the following analysis, we use a sparse k-nearest-neighbor graph with Gaussian kernel weights,

$$w_{ij} = \exp\left(-\frac{\|\mathbf{s}_i - \mathbf{s}_j\|^2}{h^2}\right) \frac{\mathbf{1}\{j \in \mathcal{N}(i)\} + \mathbf{1}\{i \in \mathcal{N}(j)\}}{2}.$$

Here, $\mathcal{N}(i)$ denotes the set of k-nearest neighbors of cell i, and $h > 0$ is a bandwidth parameter controlling how rapidly the edge weight decays with spatial distance. This symmetrization construction yields an undirected graph and provides a more balanced representation of neighborhood relationships by emphasizing mutually supported connections while down-weighting one-sided connections.

Based on the weighted adjacency matrix, we subsequently construct the graph Laplacian matrix as $\mathbf{L} = \mathbf{D} - \mathbf{W}$, where $\mathbf{D}$ is the degree matrix with $D_{ii} = \sum_j w_{ij}$ for $i = 1, \ldots, n$. The graph Laplacian matrix captures the connectivity structure of the spatial graph and provides a spectral description of cell-to-cell relationships. Let $\mathbf{L}\mathbf{u}_k = \lambda_k \mathbf{u}_k$, with $0 = \lambda_1 \leq \lambda_2 \leq \cdots \leq \lambda_k \leq \cdots \leq \lambda_n$, where λ_k is the k-th eigenvalue and $\mathbf{u}_k$ is the corresponding n-dimensional eigenvector. The eigenvectors associated with smaller eigenvalues vary smoothly over the graph and therefore capture broad and large-scale spatial patterns, whereas the eigenvectors associated with larger eigenvalues tend to reflect more localized or higher-frequency variation. In this sense, the eigenvectors of the graph Laplacian matrix form a candidate set of geometry-aware basis functions that adaptively characterize the observed tissue structure.

2.2 The GeoSVG-3D model

Using the spectral basis induced by the spatial graph, we next develop a *geometry-aware representation* for gene-specific spatial effects. Unlike two-dimensional ST data, three-dimensional data additionally capture gene expression variation along the axis perpendicular to the tissue-section plane, which leads to a more complex spatial geometry. This makes it difficult for a fixed

parametric form of spatial variation to adequately characterize irregular spatial patterns in real tissues. Therefore, we use a data-driven representation based on graph-derived basis functions to capture expression variation from the observed adjacency structure of cells in a more flexible manner.

Specifically, since eigenvectors associated with larger eigenvalues may be more sensitive to local perturbations or noise, we select the first K nontrivial eigenvectors of the graph Laplacian matrix, $\{\mathbf{u}_k : k = 1, \ldots, K\}$, as spatial components, corresponding to the K smallest nonzero eigenvalues. For each gene g, the latent spatial effect at cell i is then specified through the basis expansion, $f_g(\mathbf{s}_i) = \sum_{k=1}^{K} \theta_{gk} u_k(i)$, where $u_k(i)$ denotes the i-th entry of $\mathbf{u}_k$ and θ_{gk} is the gene-specific coefficient for the k-th basis function. The resulting expression model is given by

$$\begin{aligned} y_{ig} &= \mu_g + f_g(\mathbf{s}_i) + \epsilon_{ig} \\ &= \mu_g + \sum_{k=1}^{K} \theta_{gk} u_k(i) + \epsilon_{ig}, \quad i = 1, \ldots, n. \end{aligned} \tag{1}$$

where μ_g denotes the gene-specific baseline expression and ϵ_{ig} accounts for residual variation, with ϵ_{ig} independently following the normal distribution $N(0, \sigma_g^2)$ with zero mean and variance σ_g^2. Under model (1), if gene g is an SVG, its spatial pattern embedded in the expression profile can be represented by a nonzero linear combination of the basis functions; equivalently, at least one coefficient θ_{gk} is nonzero. In contrast, for a gene whose expression does not exist spatial pattern, the observed expression variation is mainly attributed to random noise or non-spatial factors, corresponding to all spatial-basis coefficients being zero. Thus, SVG detection is directly reduced to determining whether any coefficient in $(\theta_{g1}, \ldots, \theta_{gK})$ is nonzero.

To address this selection task in the Bayesian framework, we incorporate the neuronized prior into the coefficient specification. For each gene g and basis component k, we introduce an intermediate sparse coefficient,

$$\theta_{gk}^* = T(\xi_{gk} - \xi_{g0})\omega_{gk}, \quad k = 1, \ldots, K.$$

Here, the function $T(\cdot)$ is a non-decreasing activation function, ξ_{gk} controls whether the k-th component is activated, and ω_{gk} determines the magnitude of the coefficient once activated. Following the neuronized prior specification of Shin and Liu (2022), we assign ξ_{gk} a standard normal distribution $N(0, 1)$ and ω_{gk} a normal prior $N(0, \tau_{\omega,g}^2)$. The threshold parameter ξ_{g0} is treated as a fixed sparsity-controlling parameter.

By choosing different activation functions, the neuronized prior can recover or approximate several commonly used sparse prior behaviors, including Bayesian Lasso-type shrinkage, horseshoe-type shrinkage, and spike-and-slab-type selection. In this way, the neuronized component determines whether each graph basis function is active and provides a flexible mechanism for coefficient-level sparsity, which enables SVG detection to be formulated as Bayesian variable selection over spatial-basis coefficients.

To further incorporate graph-frequency information, we apply a frequency-dependent scaling factor motivated by the stochastic partial differential equation representation of spatial fields

(Lindgren et al., 2011). Specifically, we specify the spatial-basis coefficients as

$$\theta_{gk} = s_{gk}\theta^*_{gk}, \quad s_{gk} = (\kappa_g^2 + \lambda_k)^{-\alpha_g/2}.$$

Here, λ_k is the eigenvalue associated with the k-th basis function $\mathbf{u}_k$ and is interpreted as the corresponding graph frequency. The parameter κ_g controls the decay rate of spectral weights across graph frequencies, while the smoothness parameter α_g determines the strength of penalization on high-frequency components. This spectral scaling term s_{gk} simultaneously assigns larger prior variability to low-frequency modes and assigns stronger shrinkage to localized high-frequency fluctuations. In this way, the geometry-aware basis representation allows different genes to represent their unique spatial variation through combinations of graph-derived components.

Combining the above components, we finally arrive at the GeoSVG-3D model,

$$\begin{aligned} y_{ig} &= \mu_g + \sum_{k=1}^{K} \theta_{gk} u_k(i) + \epsilon_{ig}, \quad i = 1, \ldots, n, \\ \theta_{gk} &= s_{gk}\theta^*_{gk}, \quad s_{gk} = (\kappa_g^2 + \lambda_k)^{-\alpha_g/2}, \quad \theta^*_{gk} = T(\xi_{gk} - \xi_{g0})\omega_{gk}, \quad k = 1, \ldots, K. \end{aligned} \tag{2}$$

Under the model (2), distinct spatial components $(\mathbf{u}_1, \ldots, \mathbf{u}_K)$ are employed to collectively represent the complex three-dimensional expression patterns, while irrelevant components are suppressed through the neuronized shrinkage structure. Thus, the proposed model detects SVGs by inferring whether all spatial-basis coefficients $(\theta_{g1}, \ldots, \theta_{gK})$ are shrunk toward zero or whether at least one coefficient provides evidence of location-associated expression heterogeneity.

3 Bayesian inference

3.1 Prior specification

We now assign prior distributions to the parameters in the GeoSVG-3D model. To express the prior structure more clearly, we rewrite the formulation (2) in matrix form. Equivalently, after substituting the representation of θ_{gk} into the observation model, we have

$$\mathbf{y}_g = \mu_g \mathbf{1}_n + \mathbf{B}\mathbf{Z}_g(\boldsymbol{\xi}_g)\boldsymbol{\omega}_g + \boldsymbol{\epsilon}_g, \quad \boldsymbol{\epsilon}_g \sim N(\mathbf{0}, \sigma_g^2 \mathbf{I}_n).$$

Here, $\mathbf{1}_n$ denotes the n-dimensional vector of ones and $\mathbf{I}_n$ denotes the $n \times n$ identity matrix. We denote $\boldsymbol{\omega}_g = (\omega_{g1}, \ldots, \omega_{gK})^\top$, $\boldsymbol{\xi}_g = (\xi_{g0}, \xi_{g1}, \ldots, \xi_{gK})^\top$, and $\boldsymbol{\epsilon}_g = (\epsilon_{1g}, \ldots, \epsilon_{ng})^\top$ as the vectors of coefficient gene-specific coefficient magnitudes, threshold and activation parameters in the neuronized prior, and residual errors, respectively. The $n \times K$ matrix $\mathbf{B} = (\mathbf{u}_1, \ldots, \mathbf{u}_K)$ denotes the graph-derived basis matrix, whose columns are the selected Laplacian eigenvectors. The $K \times K$ diagonal matrix $\mathbf{Z}_g(\boldsymbol{\xi}_g)$ is defined as $\mathbf{Z}_g(\boldsymbol{\xi}_g) = \mathrm{diag}(z_{g1}, \ldots, z_{gK})$, where $z_{gk} = (\kappa_g^2 + \lambda_k)^{-\alpha_g/2} T(\xi_{gk} - \xi_{g0})$ for $k = 1, \ldots, K$. Each diagonal entry z_{gk} combines the frequency-dependent scaling factor $(\kappa_g^2 + \lambda_k)^{-\alpha_g/2}$ with the neuronized activation term $T(\xi_{gk} - \xi_{g0})$ for the k-th spatial component. Recall that we set $\xi_{gk} \sim N(0, 1)$ and $\omega_{gk} \sim N(0, \tau^2_{\omega,g})$. For the remaining parameters, we assign μ_g a normal distribution $N(\eta_g, \tau^2_{\mu,g})$, and we give σ_g^2 an inverse

gamma prior Inv-Ga(ζ_g, ν_g), where ζ_g and ν_g denote the shape and scale parameters, respectively.

3.2 Posterior sampling

We employ the Markov chain Monte Carlo (MCMC) algorithm for subsequent posterior sampling. In particular, for each gene g, as ω_{gk} and ξ_{gk} are strongly correlated to a posterior, updating ξ_{gk} conditioning on ω_{gk} may result in poor mixing (Shin and Liu, 2022). Thus, we update ξ_{gk} using a Metropolis-Hastings (MH) step after marginalizing out ω_{gk}, and then update ω_{gk} from its conditional normal distribution. The specific procedure is provided as follows.

(a) For $k = 1, \ldots, K$, sequentially update the pair (ξ_{gk}, ω_{gk}). Let $A_{gk}(\xi) = \frac{s_{gk}^2 T^2(\xi - \xi_{g0})}{\sigma_g^2} + \frac{1}{\tau_{\omega,g}^2}$, and define the partial residual $\mathbf{r}_{gk} = \mathbf{y}_g - \mu_g \mathbf{1}_n - \sum_{j=1, j\neq k}^{K} s_{gj} T(\xi_{gj} - \xi_{g0}) \omega_{gj} \mathbf{u}_j$. After marginalizing out ω_{gk}, the full conditional density of ξ_{gk} is proportional to

$$p\left(\xi_{gk} \mid \mu_g, \tau_{\omega,g}^2, \sigma_g^2, \mathbf{y}_g, \boldsymbol{\omega}_{g,-k}, \boldsymbol{\xi}_{g,-k}\right) \propto A_{gk}(\xi_{gk})^{-1/2} \exp\left\{\frac{s_{gk}^2 T^2(\xi_{gk} - \xi_{g0})(\mathbf{u}_k^\top \mathbf{r}_{gk})^2}{2\sigma_g^4 A_{gk}(\xi_{gk})} - \frac{1}{2}\xi_{gk}^2\right\},$$

where $\boldsymbol{\omega}_{g,-k}$ denotes the vector of coefficient-magnitude variables excluding ω_{gk}, and $\boldsymbol{\xi}_{g,-k}$ denotes the collection of neuronized activation variables excluding ξ_{gk}, with the threshold parameter ξ_{g0} kept fixed in this conditional update.

To implement the MH update, we generate a random-walk proposal $\xi_{gk}^* \sim N(\xi_{gk}, \tau_{0,gk}^2)$, centered at the current value of ξ_{gk}. The proposed value ξ_{gk}^* is then accepted with probability $\min(1, r)$, where

$$r = \frac{A_{gk}(\xi_{gk}^*)^{-1/2} \exp\left[\frac{s_{gk}^2 T^2(\xi_{gk}^* - \xi_{g0})(\mathbf{u}_k^\top \mathbf{r}_{gk})^2}{2\sigma_g^4 A_{gk}(\xi_{gk}^*)} - \frac{1}{2}(\xi_{gk}^*)^2\right]}{A_{gk}(\xi_{gk})^{-1/2} \exp\left[\frac{s_{gk}^2 T^2(\xi_{gk} - \xi_{g0})(\mathbf{u}_k^\top \mathbf{r}_{gk})^2}{2\sigma_g^4 A_{gk}(\xi_{gk})} - \frac{1}{2}\xi_{gk}^2\right]}.$$

Given the updated value of ξ_{gk}, we sample ω_{gk} from the normal distribution,

$$\omega_{gk} \mid \xi_{gk}, \boldsymbol{\xi}_{g,-k}, \boldsymbol{\omega}_{g,-k}, \mu_g, \sigma_g^2, \tau_{\omega,g}^2, \mathbf{y}_g \sim N\left(\frac{s_{gk} T(\xi_{gk} - \xi_{g0})(\mathbf{u}_k^\top \mathbf{r}_{gk})}{\sigma_g^2 A_{gk}(\xi_{gk})},\ A_{gk}(\xi_{gk})^{-1}\right).$$

(b) Update μ_g by sampling from the normal distribution, $\mu_g \mid \boldsymbol{\omega}_g, \boldsymbol{\xi}_g, \sigma_g^2, \mathbf{y}_g \sim \mathrm{N}(\tilde{\eta}_g, \tilde{\tau}_{\mu,g}^2)$, where $\tilde{\tau}_{\mu,g}^2 = (n/\sigma_g^2 + 1/\tau_{\mu,g}^2)^{-1}$ and $\tilde{\eta}_g = \tilde{\tau}_{\mu,g}^2 \left(\mathbf{1}_n^\top (\mathbf{y}_g - \mathbf{B}\mathbf{Z}_g(\boldsymbol{\xi}_g)\boldsymbol{\omega}_g)/\sigma_g^2 + \eta_g/\tau_{\mu,g}^2\right)$.

(c) Sample σ_g^2 from its conditional inverse gamma distribution, $\sigma_g^2 \mid \mu_g, \boldsymbol{\omega}_g, \boldsymbol{\xi}_g, \mathbf{y}_g \sim$ Inv-Ga$(\tilde{\zeta}_g, \tilde{\nu}_g)$ with $\tilde{\zeta}_g = \zeta_g + \frac{n}{2}$ and $\tilde{\nu}_g = \nu_g + \frac{1}{2}\left\|\mathbf{y}_g - \mu_g \mathbf{1}_n - \mathbf{B}\mathbf{Z}_g(\boldsymbol{\xi}_g)\boldsymbol{\omega}_g\right\|^2$, where $\|x\|$ denotes the Euclidean norm of a vector x, so that $\|x\|^2 = x^\top x$.

After obtaining MCMC posterior samples, we identify SVGs by controlling the Bayesian false discovery rate (FDR) (Newton et al., 2004). Let $\boldsymbol{\theta}_g = (\theta_{g1}, \ldots, \theta_{gK})$ denote the vector of spatial-basis coefficients of gene g. If $\boldsymbol{\theta}_g = \mathbf{0}$, gene g has no spatially structured expression pattern; otherwise, gene g exhibits location-associated expression heterogeneity. We first compute the posterior probability that gene g has no spatial effect, denoted by $p_{0g} = \mathbb{P}(\boldsymbol{\theta}_g = \mathbf{0} \mid \mathbf{y}_g)$.

Let $\{\boldsymbol{\theta}_g^{(m)} : m = 1, \ldots, M\}$ denote the M posterior samples of $\boldsymbol{\theta}_g$. Then p_{0g} is estimated by the proportion of posterior samples in which all spatial-basis coefficients are zero, that is, $\widehat{p}_{0g} = \frac{1}{M}\sum_{m=1}^{M} \mathbb{I}\{\boldsymbol{\theta}_g^{(m)} = \mathbf{0}\}$. For a threshold ν, the Bayesian FDR is calculated by

$$\mathrm{FDR}(\nu) = \frac{\sum_{g=1}^{G} \widehat{p}_{0g}\mathbb{I}(\widehat{p}_{0g} < \nu)}{\sum_{g=1}^{G} \mathbb{I}(\widehat{p}_{0g} < \nu)}.$$

Given a prespecified Bayesian FDR level α_{FDR}, we choose the largest threshold $\nu^* = \sup\{\nu : \mathrm{FDR}(\nu) \leq \alpha_{\mathrm{FDR}}\}$. The final set of detected SVGs is then defined as $\widehat{\mathcal{S}} = \{g : \widehat{p}_{0g} < \nu^*\}$.

4 Simulation

We generate the synthetic data for $n = 10{,}000$ cells. For each cell i ($i = 1, \ldots, n$), the three dimensions of the spatial coordinate are independently sampled from a uniform distribution, $s_{i1}, s_{i2}, s_{i3} \sim \mathrm{U}(0, 1)$. Expression data for $G = 1{,}000$ genes are simulated, among which 120 genes are prespecified as true SVGs and the remaining 880 genes are not SVGs. For SVGs, the underlying true expression value is generated as $y_{ig} = \mu_g + f_g(\mathbf{s}_i) + \epsilon_{ig}$, where $\epsilon_{ig} \sim N(0, 0.01)$. The spatial effect function f_g is specified by four types of spatial patterns, including gradient, periodic, Gaussian-localized, and complex spatial patterns. For the first three types, we first generate an intermediate function h_g and then center it across all cells to obtain $f_g(\mathbf{s}_i) = h_g(\mathbf{s}_i) - \frac{1}{n}\sum_{m=1}^{n} h_g(\mathbf{s}_m)$. The specific forms of h_g are given as follows.

- The gradient patterns are generated from $h_g^{\mathrm{grad}}(\mathbf{s}_i) = \mathbf{d}_g^\top \mathbf{s}_i + 0.15 \sin(2\pi w_{ig} + \phi_g)$, where $\mathbf{d}_g$ is a unit vector specifying the direction of the gradient, $\phi_g \in \{0, \pi/2\}$, and w_{ig} is selected from $w_i^{(1)} = s_{i3} + 0.10\sin(2\pi s_{i1}) + 0.08\cos(2\pi s_{i2})$ and $w_i^{(2)} = s_{i3} + 0.10\sin(2\pi(s_{i1} + s_{i2}))$.
- The periodic patterns are generated from $h_g^{\mathrm{per}}(\mathbf{s}_i) = \sin(2\pi r_g u_{ig} + \phi_g + 0.25\sin(2\pi w_i^{(1)}))$, where $r_g \in \{1, 2, 3\}$, ϕ_g is a phase parameter, and $u_{ig} = (\mathbf{d}_g^\top \mathbf{s}_i - \min_m(\mathbf{d}_g^\top \mathbf{s}_m))/(\max_m \left(\mathbf{d}_g^\top \mathbf{s}_m\right) - \min_m \left(\mathbf{d}_g^\top \mathbf{s}_m\right))$.
- The Gaussian-localized patterns are generated from $h_g^{\mathrm{Gau}}(\mathbf{s}_i) = \rho_g \exp(-\sum_{j=1}^{3} \frac{(s_{ij} - c_{jg}(s_{i3}))^2}{2\sigma_{jg}^2})$, where $\mathbf{c}_g(s_{i3}) = (c_{1g}(s_{i3}), c_{2g}(s_{i3}), s_{i3})$ is the center of the localized region varying along the s_3-axis.
- The complex patterns are designed to mimic more complicated forms of three-dimensional spatial variation, such as hotspot contrasts and shell- or ring-shaped enrichment.

Each spatial pattern contains 30 genes. For the remaining genes, the spatial effect term is omitted, and the expression is generated as $y_{ig} = \mu_g + \epsilon_{ig}$. The true value of μ_g is set to 0 for all genes. Finally, we exponentiate y_{ig} to obtain continuous and positive expression data, mimicking preprocessed expression measurements.

To implement the two methods, we use fixed implementation settings throughout this paper, including both the simulation study and real data analysis. For GeoSVG-3D, the spatial graph is constructed from the three-dimensional coordinates using a k-nearest-neighbor graph with $k = 100$, and the bandwidth parameter h in the Gaussian kernel weight is set to the median of all

k-nearest-neighbor distances. We then compute the graph Laplacian matrix and select the first $K = 5$ nontrivial eigenvectors as graph-derived basis functions. For the spectral scaling factor $s_{gk} = (\kappa_g^2 + \lambda_k)^{-\alpha_g/2}$, we set $\alpha_g = 10$ and $\kappa_g = 0$, so that the prior scaling is fully determined by the graph Laplacian spectrum. This choice removes an additional range parameter and enforces stronger shrinkage on high-frequency graph components. For the prior specification, we use the ReLU activation function in the neuronized prior, corresponding to a spike-and-slab-type discrete prior, set $\xi_{g0} = 0$, and fix $\tau^2_{\omega,g} = 1$. We run 4,000 MCMC iterations with the first 2,000 discarded as burn-in steps. After posterior sampling, the Bayesian FDR is calculated based on the MCMC samples, and SVGs are selected at the target level $\alpha_{\mathrm{FDR}} = 0.05$. For scBSP, we use the gene-level p-value reported by its testing procedure, denoted by p_g^{sc}. This p-value is computed as the right-tail probability of the observed weighted ratio between large- and small-patch local mean-expression variances under a fitted log-normal null distribution. Following the significance threshold used in the scBSP analysis framework, genes are identified as SVGs if their one-sided p_g^{sc} values are less than 0.05.

Subsequently, we evaluate the detection performance by comparing the selected SVGs with the prespecified ground truth. Let TP, FP, FN, and TN denote the numbers of true positives, false positives, false negatives, and true negatives, respectively. Power is defined as $\mathrm{TP}/(\mathrm{TP}+\mathrm{FN})$, measuring the proportion of true SVGs that are successfully detected, and precision is defined as $\mathrm{TP}/(\mathrm{TP}+\mathrm{FP})$, measuring the proportion of detected SVGs that are truly spatially variable. We also generate the receiver operating characteristic (ROC) curves and compute the corresponding area under the curve (AUC) for each method to assess the threshold-free detection performance. To construct the ROC curves, genes are ranked according to method-specific detection scores. For GeoSVG-3D, we use $1 - \widehat{p}_{0g}$ as the detection score, where larger values indicate stronger posterior evidence for spatial variation. For scBSP, we use $1 - p_g^{\mathrm{sc}}$, so that larger values likewise correspond to stronger evidence for spatial variation.

Table 1: Simulation detection performance under the default decision rules. GeoSVG-3D selects SVGs by controlling Bayesian FDR at 0.05, whereas scBSP selects genes with $p_g^{\mathrm{sc}} < 0.05$. The empirical FDR is defined as $FP/(TP+FP)$.

Method	TP	FP	FN	TN	Power	Precision	empirical FDR
GeoSVG-3D	120	33	0	847	1.000	0.784	0.216
scBSP	106	49	14	831	0.883	0.684	0.316

The overall SVG detection performance is summarized in Table 1. GeoSVG-3D identifies 153 genes as SVGs, including all 120 true SVGs and 33 false positives, corresponding to a power of 1.000 and a precision of 0.784. In comparison, scBSP identifies 155 genes as SVGs, including 106 true positives and 49 false positives, yielding a power of 0.883 and a precision of 0.684. We further evaluate the two methods using ROC curves, as shown in Figure 1 (a). GeoSVG-3D achieves an AUC of 0.9998, whereas scBSP achieves an AUC of 0.9778. These results indicate that both methods recover a large proportion of true SVGs, while GeoSVG-3D detects all true SVGs and achieves higher precision in this simulation setting. Figures 1(b)-(f) also show representative simulated expression patterns from the four SVG classes, including smooth gradient variation, periodic variation, localized enrichment, and more irregular three-dimensional structures. These examples illustrate that the simulated SVGs cover both simple

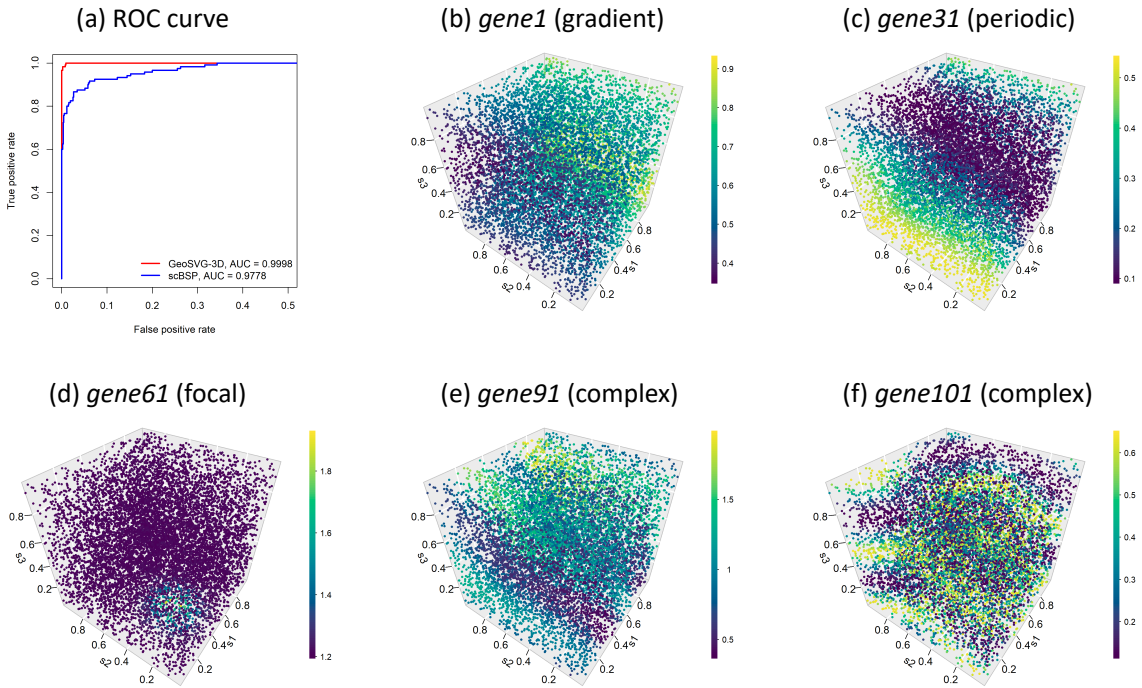

Figure 1: Performance comparison and representative simulated spatial expression patterns. (a) ROC curves for SVG detection by GeoSVG-3D and scBSP. (b)-(f) Representative simulated expression patterns, including a gradient pattern, a periodic pattern, a focal pattern, and two complex patterns. The colors represent the observed simulated expression values after transformation.

and challenging spatial expression patterns.

To further characterize the performance difference between the two methods, we examine the 14 true SVGs that are not detected by scBSP. Among them, 12 genes correspond to the focal patterns and 2 genes correspond to the gradient patterns. This indicates that, in this simulation setting, the power loss of scBSP occurs predominantly for localized three-dimensional spatial signals. In particular, the focal patterns are confined to only a small portion of the spatial domain, and their contrast with the background may therefore be attenuated when local mean-expression variation is aggregated across spatial patches. In contrast, GeoSVG-3D recovered all true SVGs, suggesting higher sensitivity to localized spatial variation and more accurate identification of spatially variable signals under the current simulation setting.

5 Real application

In this section, we apply GeoSVG-3D and scBSP to a three-dimensional mouse brain ST dataset generated by the Deep-STARmap technology. Deep-STARmap enables three-dimensional in situ quantification of thousands of gene transcripts within thick mouse brain tissue blocks, while preserving cell-level spatial coordinates (Sui et al., 2025). The dataset contains an expression matrix of 1,017 genes measured across 198,675 cells, along with their three-dimensional spatial coordinates. The cell-type annotations were obtained from the FUSEmap labels provided by the Deep-STARmap study, where FUSEmap integrates spatial transcriptomic profiles with reference

mouse brain atlases to assign molecular cell-type identities (He et al., 2024). To reduce the effect of cell-type composition and focus on within-cell-type spatial expression variation, the subsequent analysis is performed within a single cell type, peptidergic neurons, based on the FUSEmap main-level annotations. The dataset is available at https://zenodo.org/records/16783355.

We preprocess the raw gene expression data using a standard procedure. First, cells with zero total count and genes detected in fewer than one cell are removed. For each remaining cell, library-size normalization is performed by scaling its total expression count to 10^4. The $\log(1+x)$ transformation is then applied to obtain the preprocessed expression value. The final expression matrix contains 9,212 cells and 1,017 genes. Next, we impute the gene expression data to reduce excessive zero values, which may arise from technical artifacts or transcript-capture limitations and thereby reduce the stability of SVG detection. Here, we use STAGATE to perform imputation by reconstructing gene expression profiles using shared information from spatially neighboring and transcriptionally similar cells (Dong and Zhang, 2022). The zero value proportion decreases from 0.953 before STAGATE reconstruction to 0.101 thereafter. The spatial coordinates are scaled to $[0,1]\times[0,1]\times[0,1]$ and used as the input for GeoSVG-3D. For scBSP, the raw count data and cell coordinates are input directly.

To implement GeoSVG-3D, we carry out 4,000 MCMC iterations with the first 2,000 as burn-in. Based on the posterior samples after burn-in, SVGs are selected by controlling the Bayesian FDR at the 0.05 level, resulting in 341 detected SVGs. For these SVGs, we conduct pathway analysis to assess their biological functions using the Gene Set Enrichment Analysis platform and the Gene Ontology dataset available on the Broad Institute website (http://software.broadinstitute.org/gsea/msigdb/annotate.jsp). The names of the 341 SVGs and their associated pathways are provided in Supplementary Table S1 and S2. The results show that these SVGs are significantly enriched in pathways associated with neuronal function and structure, including neuronal projection, neuropeptide signaling, and cell-cell communication. In particular, the enrichment of the neuropeptide signaling pathway is consistent with the biological characteristics of the analyzed peptidergic neuronal population. These results suggest that the genes detected by GeoSVG-3D show functional coherence and represent spatially variable signals related to specific neuronal functions. For comparison, scBSP identifies 170 SVGs under the significance criterion $p_g^{\mathrm{sc}} < 0.05$. Among the detected genes, 70 are identified as SVGs by both methods, indicating a shared subset of spatially variable signals as well as method-specific discoveries.

Next, we randomly choose nine SVGs detected with $\widehat{p}_{0g} = 0$ to exhibit their spatial patterns (Figure 2). The selected genes exhibit clear three-dimensional expression heterogeneity within the peptidergic neurons subset, which forms localized or regionally enriched structures along the tissue geometry. In particular, *Adcyap1r1*, *Adora1*, *Alcam*, *Calb2*, *Cbln4*, and *Gpx3* show relatively restricted or column-like enriched domains, whereas *Clu* and *Hap1* exhibit broader spatially organized expression across a larger portion of the region. *Dkk3* shows a sparser and localized pattern, with expression concentrated in limited subregions. In greater detail, *Adcyap1r1* shows relatively high expression in the middle-to-upper region along the s_3-axis, whereas the high-expression regions of *Adora1* and *Clu* are mainly concentrated around the

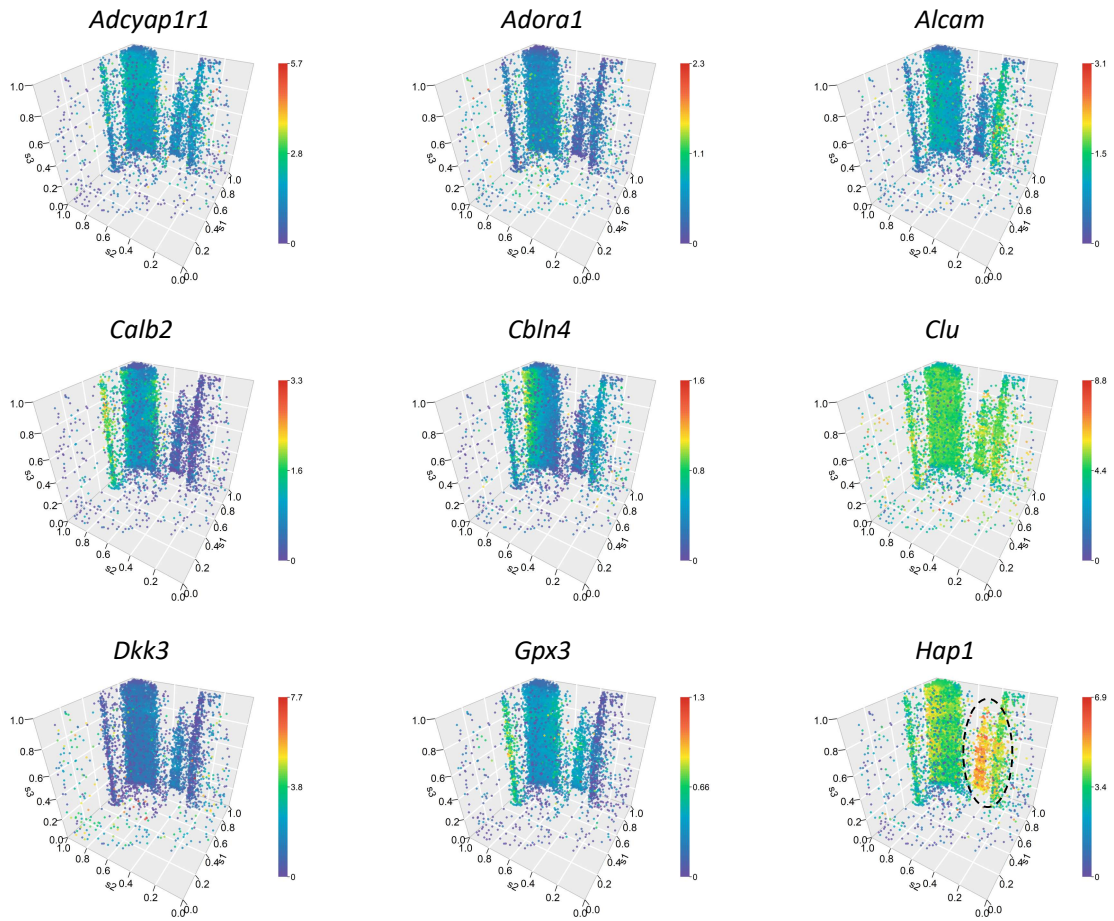

Figure 2: Three-dimensional spatial expression patterns of representative SVGs detected in the peptidergic neurons subset. Values represent preprocessed and STAGATE-imputed expression data.

middle of the s_3-axis. *Alcam* shows relatively high expression primarily in the middle-to-lower part of the rightmost column-like region. *Calb2* and *Gpx3* exhibit similar spatial distributions, with high expression concentrated in the middle-to-upper part of the left column-like region and gradually decreasing toward the surrounding areas. In contrast, *Cbln4* and *Dkk3* show no clear overall trend along the s_3-axis but exist distinct spatial variation within the s_1s_2 plane, indicating that their spatial heterogeneity is mainly expressed in the planar directions. *Hap1* shows strong local enrichment, with its high-expression region mainly confined to the tapered, shoot-like region outlined by the dashed line.

To better visualize spatial variation within the s_1s_2 plane, we display all cells on a common plane according to their s_1 and s_2 coordinates. The corresponding expression distributions of the nine genes selected above are shown in Figure 3. Overall, *Adcyap1r1*, *Clu*, and *Hap1* exhibit a similar large-scale trend, with their expression levels increasing approximately from the lower-left to the upper-right. Superimposed on this trend, *Hap1* shows a localized high-expression region within the dashed domain on the right, where *Clu* also exhibits relatively high expression, but this local enrichment is less evident for *Adcyap1r1*. In contrast to these broad spatial trends, the remaining genes exhibit more localized or region-specific enrichment. The high-expression

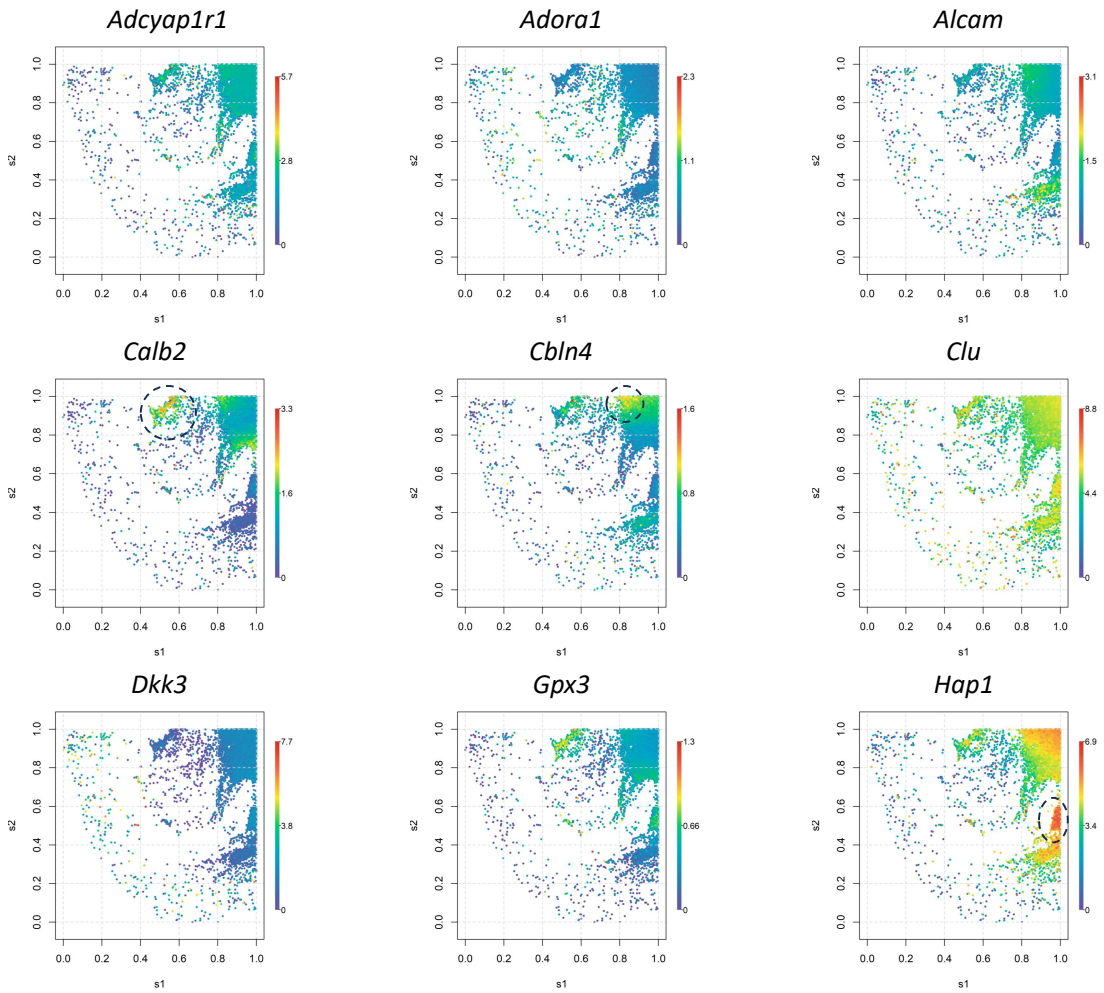

Figure 3: s_1s_2-plane projections of representative SVGs detected in the peptidergic neurons subset. Colors represent preprocessed and STAGATE-imputed expression values. These projections complement the three-dimensional views in Figure 2 by highlighting spatial variation within the s_1s_2 plane.

signal of *Adora1* is concentrated mainly in the central area of the plane, whereas that of *Alcam* is located primarily in the lower-right region. The expression of *Calb2* is highly concentrated within the dashed domain, and *Gpx3* exhibits a similar localized high-expression pattern in the same area. *Cbln4* also shows localized enrichment, but its high-expression signal is concentrated within a different dashed domain in the upper-right region, accompanied by moderately elevated expression in the lower-right region. Finally, *Dkk3* displays a distinct spatial pattern, with its high-expression signal mainly distributed along the sparse band-like region on the lower-left side and relatively low expression in the central area.

Furthermore, several genes detected by GeoSVG-3D have been implicated in brain function and tissue organization in previous biological studies. For example, *Chrm1* encodes a receptor involved in acetylcholine signaling and has been linked to cortical function, cognition, and neurological disorders (Dean and Scarr, 2021). *Cacna2d2* is involved in calcium-channel function, and its loss in mice leads to cerebellar ataxia and increased seizure susceptibility, suggesting relevance to neuronal dysfunction (Ivanov et al., 2004). GeoSVG-3D also detects genes related to local tissue organization and cell identity. *Alcam* is involved in cell adhesion and axonal growth,

suggesting that its spatial variation may reflect local differences in the cellular microenvironment (Bye et al., 2019). *Calb2* encodes calretinin, a commonly used marker for a subset of inhibitory interneurons in the mouse cortex, where calretinin-expressing neurons are enriched in upper cortical layers (Camillo et al., 2018; Medalla et al., 2023). Taken together, these representative genes suggest that the SVGs identified by GeoSVG-3D capture biologically meaningful spatial variation related to neuronal function, disease relevance, and local tissue organization.

6 Discussion

In this paper, we propose a geometry-aware Bayesian framework GeoSVG-3D for detecting SVGs in three-dimensional ST data. GeoSVG-3D constructs a weighted spatial graph from cell coordinates and uses the corresponding graph Laplacian eigenvectors as data-driven basis functions for modeling gene-specific spatial effects. Within this representation, the stochastic partial differential equation-inspired spectral scaling regularizes graph-frequency components, while neuronized priors impose sparsity on the basis coefficients. Posterior samples are then used to quantify gene-level spatial evidence and perform Bayesian FDR control for SVG selection. Both the simulation study and real data analysis demonstrate that GeoSVG-3D can identify genes with structured spatial expression variation in three-dimensional tissue space.

The main advantage of GeoSVG-3D is reflected in its integration of adaptive geometry-aware modeling and Bayesian variable selection. By deriving basis functions from the observed tissue geometry, GeoSVG-3D avoids specifying a fixed functional form for spatial effects and can adapt to unknown spatial patterns through cell-to-cell adjacency encoded in the graph. The spectral scaling term further distinguishes smooth low-frequency components from overly local high-frequency fluctuations, helping preserve meaningful spatial structures while reducing sensitivity to local noise. Meanwhile, neuronized priors select active spatial components for each gene and provide posterior uncertainty quantification. By aggregating coefficient-level evidence into the posterior probability of no spatial effect, GeoSVG-3D yields a valid Bayesian FDR-based procedure for identifying SVGs.

References

Mikhail Belkin and Partha Niyogi. Laplacian eigenmaps for dimensionality reduction and data representation. *Neural Computation*, 15(6):1373–1396, 2003.

Mikhail Belkin and Partha Niyogi. Convergence of Laplacian eigenmaps. *Advances in Neural Information Processing Systems*, 19, 2006.

Christopher R Bye, Valeria Rytova, Walaa F Alsanie, Clare L Parish, and Lachlan H Thompson. Axonal growth of midbrain dopamine neurons is modulated by the cell adhesion molecule ALCAM through trans-heterophilic interactions with L1Cam, ChL1, and Semaphorins. *Journal of Neuroscience*, 39(34):6656–6667, 2019.

Dylan M Cable, Evan Murray, Vignesh Shanmugam, Simon Zhang, Luli S Zou, Michael Diao,

Haiqi Chen, Evan Z Macosko, Rafael A Irizarry, and Fei Chen. Cell type-specific inference of differential expression in spatial transcriptomics. *Nature Methods*, 19(9):1076–1087, 2022.

Daniela Camillo, Mehran Ahmadlou, M Hadi Saiepour, Maryam Yasaminshirazi, Christiaan N Levelt, and J Alexander Heimel. Visual processing by calretinin expressing inhibitory neurons in mouse primary visual cortex. *Scientific Reports*, 8(1):12355, 2018.

Brian Dean and Elizabeth Scarr. Changes in cortical gene expression in the muscarinic m1 receptor knockout mouse: potential relevance to schizophrenia, alzheimer's disease and cognition. *npj Schizophrenia*, 7(1):44, 2021.

Kangning Dong and Shihua Zhang. Deciphering spatial domains from spatially resolved transcriptomics with an adaptive graph attention auto-encoder. *Nature Communications*, 13(1): 1739, 2022.

Jianqing Fan and Runze Li. Variable selection via nonconcave penalized likelihood and its oracle properties. *Journal of the American Statistical Association*, 96(456):1348–1360, 2001.

Rongxin Fang, Aaron Halpern, Mohammed Mostafizur Rahman, Zhengkai Huang, Zhiyun Lei, Sebastian J Hell, Catherine Dulac, and Xiaowei Zhuang. Three-dimensional single-cell transcriptome imaging of thick tissues. *Elife*, 12:RP90029, 2024.

David K Hammond, Pierre Vandergheynst, and Rémi Gribonval. Wavelets on graphs via spectral graph theory. *Applied and Computational Harmonic Analysis*, 30(2):129–150, 2011.

Yichun He, Hao Sheng, Hailing Shi, Wendy Xueyi Wang, Zefang Tang, Jia Liu, and Xiao Wang. Towards a universal spatial molecular atlas of the mouse brain. *bioRxiv*, pages 2024–05, 2024.

Jian Hu, Xiangjie Li, Kyle Coleman, Amelia Schroeder, Nan Ma, David J Irwin, Edward B Lee, Russell T Shinohara, and Mingyao Li. SpaGCN: Integrating gene expression, spatial location and histology to identify spatial domains and spatially variable genes by graph convolutional network. *Nature Methods*, 18(11):1342–1351, 2021.

Sergey V Ivanov, Jerrold M Ward, Lino Tessarollo, Dorothea McAreavey, Vandana Sachdev, Lameh Fananapazir, Melissa K Banks, Nicole Morris, Draginja Djurickovic, Deborah E Devor-Henneman, et al. Cerebellar ataxia, seizures, premature death, and cardiac abnormalities in mice with targeted disruption of the Cacna2d2 gene. *The American Journal of Pathology*, 165 (3):1007–1018, 2004.

Jinpu Li, Mauminah Raina, Yiqing Wang, Chunhui Xu, Li Su, Qi Guo, Ricardo Melo Ferreira, Michael T Eadon, Qin Ma, Juexin Wang, et al. scBSP: a fast and accurate tool for identifying spatially variable features from high-resolution spatial omics data. *Bioinformatics*, 41(10): btaf554, 2025a.

Zhijian Li, Zain M. Patel, Dongyuan Song, Sai Nirmayi Yasa, Robrecht Cannoodt, Guanao Yan, Jingyi Jessica Li, and Luca Pinello. Systematic benchmarking of computational methods to identify spatially variable genes. *Genome Biology*, 26(1):285, 2025b.

Finn Lindgren, Håvard Rue, and Johan Lindström. An explicit link between Gaussian fields and Gaussian Markov random fields: the stochastic partial differential equation approach. *Journal of the Royal Statistical Society Series B: Statistical Methodology*, 73(4):423–498, 2011.

Maria Medalla, Bingxin Mo, Rakin Nasar, Yuxin Zhou, Junwoo Park, and Jennifer I Luebke. Comparative features of calretinin, calbindin, and parvalbumin expressing interneurons in mouse and monkey primary visual and frontal cortices. *Journal of Comparative Neurology*, 531(18):1934–1962, 2023.

Peter Müller, Giovanni Parmigiani, and Kenneth Rice. FDR and Bayesian multiple comparisons rules. *Bayesian Statistics 8*, pages 359–380, 2007.

Michael A Newton, Amine Noueiry, Deepayan Sarkar, and Paul Ahlquist. Detecting differential gene expression with a semiparametric hierarchical mixture method. *Biostatistics*, 5(2):155–176, 2004.

RB O'Hara and MJ Sillanpää. A review of Bayesian variable selection methods: What, how and which. *Bayesian Analysis*, 4(1):85–118, 2009.

Anjali Rao, Dalia Barkley, Gustavo S França, and Itai Yanai. Exploring tissue architecture using spatial transcriptomics. *Nature*, 596(7871):211–220, 2021.

Marie Schott, Daniel León-Periñán, Elena Splendiani, Leon Strenger, Jan Robin Licha, Tancredi Massimo Pentimalli, Simon Schallenberg, Jonathan Alles, Sarah Samut Tagliaferro, Anastasiya Boltengagen, et al. Open-ST: High-resolution spatial transcriptomics in 3D. *Cell*, 187(15):3953–3972, 2024.

Matthias Seeger. Gaussian processes for machine learning. *International Journal of Neural Systems*, 14(02):69–106, 2004.

Minsuk Shin and Jun S Liu. Neuronized priors for bayesian sparse linear regression. *Journal of the American Statistical Association*, 117(540):1695–1710, 2022.

David I Shuman, Sunil K Narang, Pascal Frossard, Antonio Ortega, and Pierre Vandergheynst. The emerging field of signal processing on graphs: Extending high-dimensional data analysis to networks and other irregular domains. *IEEE Signal Processing Magazine*, 30(3):83–98, 2013.

Patrik L Ståhl, Fredrik Salmén, Sanja Vickovic, Anna Lundmark, José Fernández Navarro, Jens Magnusson, Stefania Giacomello, Michaela Asp, Jakub O Westholm, Mikael Huss, et al. Visualization and analysis of gene expression in tissue sections by spatial transcriptomics. *Science*, 353(6294):78–82, 2016.

Michael L Stein. *Interpolation of Spatial Data: Some Theory for Kriging*. Springer Science & Business Media, 1999.

Xin Sui, Jennifer A Lo, Shuchen Luo, Yichun He, Zefang Tang, Zuwan Lin, Dániel L Barabási, Yiming Zhou, Wendy Xueyi Wang, Jia Liu, et al. Scalable spatial single-cell transcriptomics and translatomics in 3D thick tissue blocks. *Nature Methods*, pages 1–11, 2025.

Shiquan Sun, Jiaqiang Zhu, and Xiang Zhou. Statistical analysis of spatial expression patterns for spatially resolved transcriptomic studies. *Nature Methods*, 17(2):193–200, 2020.

Valentine Svensson, Sarah A Teichmann, and Oliver Stegle. Spatialde: identification of spatially variable genes. *Nature Methods*, 15(5):343–346, 2018.

Robert Tibshirani. Regression shrinkage and selection via the lasso. *Journal of the Royal Statistical Society Series B: Statistical Methodology*, 58(1):267–288, 1996.

Ulrike Von Luxburg. A tutorial on spectral clustering. *Statistics and Computing*, 17(4):395–416, 2007.

Benjamin L Walker, Zixuan Cang, Honglei Ren, Eric Bourgain-Chang, and Qing Nie. Deciphering tissue structure and function using spatial transcriptomics. *Communications Biology*, 5 (1):220, 2022.

Gefei Wang, Jia Zhao, Yan Yan, Yang Wang, Angela Ruohao Wu, and Can Yang. Construction of a 3D whole organism spatial atlas by joint modelling of multiple slices with deep neural networks. *Nature Machine Intelligence*, 5(11):1200–1213, 2023a.

Juexin Wang, Jinpu Li, Skyler T Kramer, Li Su, Yuzhou Chang, Chunhui Xu, Michael T Eadon, Krzysztof Kiryluk, Qin Ma, and Dong Xu. Dimension-agnostic and granularity-based spatially variable gene identification using bsp. *Nature Communications*, 14(1):7367, 2023b.

Xiao Wang, William E Allen, Matthew A Wright, Emily L Sylwestrak, Nikolay Samusik, Sam Vesuna, Kathryn Evans, Cindy Liu, Charu Ramakrishnan, Jia Liu, et al. Three-dimensional intact-tissue sequencing of single-cell transcriptional states. *Science*, 361(6400):eaat5691, 2018.

Zhiwei Wang, Yeqin Zeng, Ziyue Tan, Yuheng Chen, Xinrui Huang, Hongyu Zhao, Zhixiang Lin, and Can Yang. A unified framework for identification of cell-type-specific spatially variable genes in spatial transcriptomic studies. *Proceedings of the National Academy of Sciences*, 122 (46):e2503952122, 2025.

Guanao Yan, Shuo Harper Hua, and Jingyi Jessica Li. Categorization of 34 computational methods to detect spatially variable genes from spatially resolved transcriptomics data. *Nature Communications*, 16(1):1141, 2025.

Jinge Yu and Xiangyu Luo. Identification of cell-type-specific spatially variable genes accounting for excess zeros. *Bioinformatics*, 38(17):4135–4144, 2022.

Shan Yu and Wei Vivian Li. spVC for the detection and interpretation of spatial gene expression variation. *Genome Biology*, 25(1):103, 2024.

Ming Yuan and Yi Lin. Model selection and estimation in regression with grouped variables. *Journal of the Royal Statistical Society Series B: Statistical Methodology*, 68(1):49–67, 2006.

Cun-Hui Zhang. Nearly unbiased variable selection under minimax concave penalty. *The Annals of Statistics*, 38(2):894–942, 2010.

Ran Zhou, Gaoxia Yang, Yan Zhang, and Yuan Wang. Spatial transcriptomics in development and disease. *Molecular Biomedicine*, 4(1):32, 2023.

Jiaqiang Zhu, Shiquan Sun, and Xiang Zhou. SPARK-X: non-parametric modeling enables scalable and robust detection of spatial expression patterns for large spatial transcriptomic studies. *Genome Biology*, 22(1):184, 2021.

Hui Zou and Trevor Hastie. Regularization and variable selection via the elastic net. *Journal of the Royal Statistical Society Series B: Statistical Methodology*, 67(2):301–320, 2005.